Received: 21 December 2021 | Revised: 11 April 2022 | Accepted: 14 May 2022

DOI: 10.1002/cnm.3630

BASIC RESEARCH

WILEY

Fluid structure interaction versus rigid-wall approach in the study of the symptomatic stenosed carotid artery: Importance of wall compliance and resilience of loose connective tissue

Daniel Jodko[1] | **Mateusz Jeckowski**[2] | **Zbigniew Tyfa**[1]

[1]Institute of Turbomachinery, Lodz University of Technology, Lodz, Poland

[2]Department of Experimental Surgery, Medical University of Lodz, Lodz, Poland

Correspondence
Daniel Jodko, Institute of Turbomachinery, Lodz University of Technology, Wolczanska 217/221, 93-005 Lodz, Poland.
Email: daniel.jodko@p.lodz.p

Funding information
Fund of Young Researchers granted by the Faculty of Mechanical Engineering at the Lodz University of Technology

Abstract

The purpose of this paper is to demonstrate the importance of a compliant wall approach in modeling of non-Newtonian and non-physiological blood flows. A case study of a stenosed and symptomatic carotid bifurcation was considered to show the influence of the wall-resilience assumption on the flow parameters obtained with numerical simulations. Patient-specific data concerning the geometry and flow conditions were collected and used to carry out two-way coupled fluid structure interaction simulations of the pulsatile blood flow through carotid artery. The wall compliance was considered separately as related to the wall-elasticity and as associated with the reaction of the loose connective tissue surrounding the carotid bifurcation. The obtained hemodynamic parameters were compared to those which were found in rigid-wall simulations. The difference between the results obtained for rigid-wall and compliant-wall approaches for the peak-systolic area-averaged wall shear stress achieved 35%, whereas the difference between the time-averaged local vorticity and shear strain reached, respectively, 42% and 43%. The influence of the highly resilient wall on the monitored hemodynamic parameters was significant even if time-averaged values are compared, which suggests that these metrics are considerably overestimated if the wall compliance is not considered. Moreover, the findings show that the mechanical response of the loose connective tissue cannot be neglected in blood flow simulations. Additionally, this study indicates that stiffening of the arterial wall due to atherosclerosis significantly rises hemodynamic parameters. This explains the therapeutic benefits of surgical removal of plaque lesions formed in the carotid bifurcation (endarterectomy).

KEYWORDS

carotid artery, fluid structure interaction, ischemic stroke, non-Newtonian blood, non-physiological hemodynamics, symptomatic stenosis

1 | INTRODUCTION

Atheropathogenesis, related to smoking, sedentary lifestyle, diet, and even genetic predisposition, is a serious problem rising cardiovascular morbidity and mortality and is the largest cause of death in aging populations of well-developed countries.[1,2] Atherosclerotic plaque build-up in carotid artery may form stenosis leading to an ischemic stroke associated with high blood pressure drop, plaque rupture, or clot formation. The ischemic stroke is a lack of blood circulation in the brain, which can result in death or loosing of brain functions, disability, and loss of independent life. Stenoses can be asymptomatic or symptomatic. Neurological signs can be mild like blurry vision or vertigo, although often could lead to serious neurological deficit including paresis or coma. Carotid artery stenosis, resulting from atherosclerotic plaque, is responsible for 15%–20% of all cases of stroke,[3] wherein according to Wafa et al in 2017 there were 1.12 million incident strokes in Europe with 0.46 million deaths, and 7.06 million disability-adjusted life years lost because of stroke.[4] The same authors estimate that by 2047 a number of incident strokes will increase by 40,000. The increase in the number of cases, which is enlarging patients' suffering, is also constantly rising national expenditures on public health service in numerous countries. Thus, it encourages multidisciplinary research groups to conduct thorough researches providing a deeper insight into the multifactorial process of atheropathogenesis. Carotid artery stenosis as a risk factor is surgically removable and, despite possible intraoperative complications, the intervention has positive long-term outcomes.[5]

The crucial role in the development of the plaque is played by hemodynamic conditions, mostly by oscillating and non-physiologically low or high values of wall shear stress (WSS) associated with disturbed blood flow in the vicinity of arterial branches.[6–10] Therefore, stenoses formed in the internal carotid artery (ICA), which is responsible for brain perfusion, are usually located just after the division of the common carotid artery (CCA) into ICA and external carotid artery (ECA) supplying the face and neck. Elevated wall WSS, induced by the viscous blood flow on the endothelial internal layer of blood vessel walls, cannot be directly measured in vivo, however, it can be precisely calculated with computational fluid dynamics (CFD). Thus, over the last 20 years, numerical methods have been employed by numerous researchers for modeling of blood flow in patient-specific geometries of different parts of the human circulatory system, including carotid bifurcations.[11–15]

In the majority of studies devoted to numerical modeling of blood flows in carotid artery blood vessel walls have been considered to be rigid, however, this assumption had to be accepted due to a limited computational power. In the last 10 years, a rapid development of computers, associated with an acceleration of processors, has allowed researchers to carry out computer simulations of blood flows with coupled two-way fluid structure interaction techniques (FSI), in which walls are considered to be resilient. Despite the fact that FSI calculations are time-demanding and relatively expensive while compared to the rigid-wall approach, some researchers have shown the importance of taking into account blood vessel compliance. As a result, blood pressure damping is included in numerical simulations, which significantly influences the results obtained in the fluid domain, which represents local hemodynamics. McGah et al[16] showed that the rigid wall assumption is burdened with uncertainty related to the fact that the values of WSS may be over-estimated by up to 10%. A similar overestimation of WSS (10%–13%) was found in a rigid model of an arteriovenous fistula when compared to a compliant wall analogous case presented in Reference 17. The same group showed that the rigid-wall simulation can overestimate the peak velocity by 20% and the peak WSS values by 15%[18] as compliant walls are able to accumulate a part of the mechanical energy of the fluid. The significance of this fact was shown indirectly in the FSI study devoted to an analysis of the blood flow in a carotid branch for different stages of hypertension.[19] Lopes et al[20] compared rigid-wall and compliant-wall approaches to investigate different stages of stiffening of healthy carotid walls but the authors focused mostly on flow rate distribution and areas of low WSS that prone to atheropathogenesis. Contrary, Sousa et al[21] did not find significant differences between the results obtained in analogous rigid and compliant models of the carotid bifurcation. However, Sousa et al and Lopes et al studied non-stenosed carotid artery and considered blood to be a Newtonian fluid. Thus, other parameters, such as vorticity, shear strain, or local blood viscosity, which may be relevant to pathological non-Newtonian hemodynamics in symptomatic stenosed arteries, have not been investigated.

Although wall compliance cannot be negligible, researchers conducting FSI analyses have to accept numerous assumptions related to modeling of blood vessel wall behavior. First of all, the mechanical properties of arterial tissue need to be described by a selected linear or more sophisticated model of a viscoelastic or hyperelastic material (which defines the stress–strain relationship). Moreover, the attenuation and compliance of the surrounding tissue must be taken into account. Cushioning effects can be mathematically expressed by damping coefficients. The flexibility of tissues located in the vicinity of the blood vessel (called loose connective tissue, LCT) is described by the foundation

stiffness coefficient (FS), which has to be defined. However, the problem concerning the choice of the most appropriate linear or nonlinear model describing material properties of the wall has not been resolved yet. Moreover, damping and FS remain unknown.

The novelty of this study is to show how arbitrarily selected parameters describing wall compliance and mechanical response of LCT can quantitatively affect pathological hemodynamics obtained in patient-specific FSI simulations of non-Newtonian blood flow in symptomatic carotid stenosis. The second objective of this paper is to present the significance of the resilient-wall approach in blood flow modeling as compared to the rigid-wall simplification. The presented findings may be used by other researchers investigating blood flows and can be correlated with in vivo measurements done in symptomatic stenoses formed in carotid branch areas. However, the obtained results and observations may be useful for all who do researches on flows in rubber-like tubes or pipes.

2 | MATERIAL AND METHODS

Conducting patient-specific simulations required reconstruction of the model and determination of flow conditions based on data acquisition, generation of numerical grids followed by mesh testing, bidirectional numerical FSI calculations and extraction of the obtained results. The patient-specific geometry was obtained with an approval from the Local Bioethics Committee at the Medical University of Lodz on February 18th, 2018 (RNN/63/18/KE) and in accordance with the Helsinki Declaration of 1975, as revised in 2000, the identification of the patient has been made anonymous for the publication of this paper. Prior to medical examination, the patient was fully informed and signed a consent form as per IRB protocol.

2.1 | Model reconstruction

To generate a patient-specific carotid artery model compatible with ANSYS Mesher software and suitable for the generation of the external wall, a reconstruction process comprised three main stages. The first one was related to biomedical image segmentation, extraction of patient-specific surface geometry of the arterial lumen (in a custom, in-house software developed in Institute of Turbomachinery at Lodz University of Technology), and extraction of the vessel lumen contours. The second stage involved importing the generated contours into the CAD program (computer-aided design) and generating a volumetric object via the profiles-lofting method. Since the atherosclerotic plaque was not segmented as a part of the fluid domain (it was treated as a separate object that was saved in stereolithography STL format), the authors obtained a model of the patient-specific lumen of a carotid artery bifurcation without a pathological change. Then, the authors used a ScanTo3D algorithm available in SolidWorks software to convert a surface (STL) model of atherosclerotic plaque into volumetric one. Afterwards, a standard Boolean subtraction was performed to obtain a patient-specific model of the arterial lumen, including vessel narrowing resulting from the stenosis presence. Finally, a wall of specific thickness had to be added to the existing geometry. As a result, the authors obtained two separate volumetric models, i.e. the first one mimicking blood vessel lumen, while the second representing the arterial wall. A more thorough description of this multistep geometry reconstruction technique is provided in Appendix S1. A simple workflow chart presenting the chosen stages of the model preparation is outlined in Figure 1.

2.2 | Boundary conditions and assumptions

To simulate patient-specific flow, an ultrasound examination was performed to acquire a velocity waveform that could be used to define the inlet boundary condition (Figure 2). Due to the satisfactory length of the CCA allowing the velocity profile to be developed upstream the investigated carotid bifurcation, and due to low values of the estimated Reynolds number (Re = 486 at peak systole), the idealized parabolic velocity profile was applied at the inlet cross-section: $V_p = V_{max} \cdot (1 - [r/R_{max}]^2)$. The maximal velocity V_{max} at the cross-section center was assumed to be a function of time in accordance with the curve obtained in vivo (Figure 3).

A normal blood pressure waveform representing the peripheral resistance, employed in another FSI study,[19] was time-integrated with the velocity function and applied at both outlet cross-sections as the outlet boundary condition.

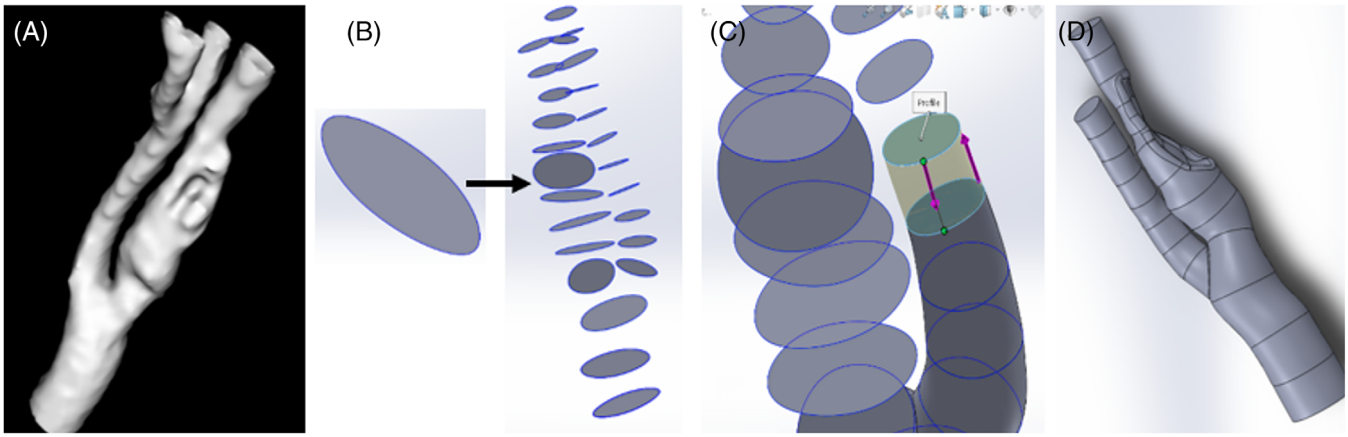

FIGURE 1 Patient-specific geometry: (A) surface model obtained in the custom-developed software Anatomical Model Reconstructor; (B–D) volumetric model retrieved in SolidWorks

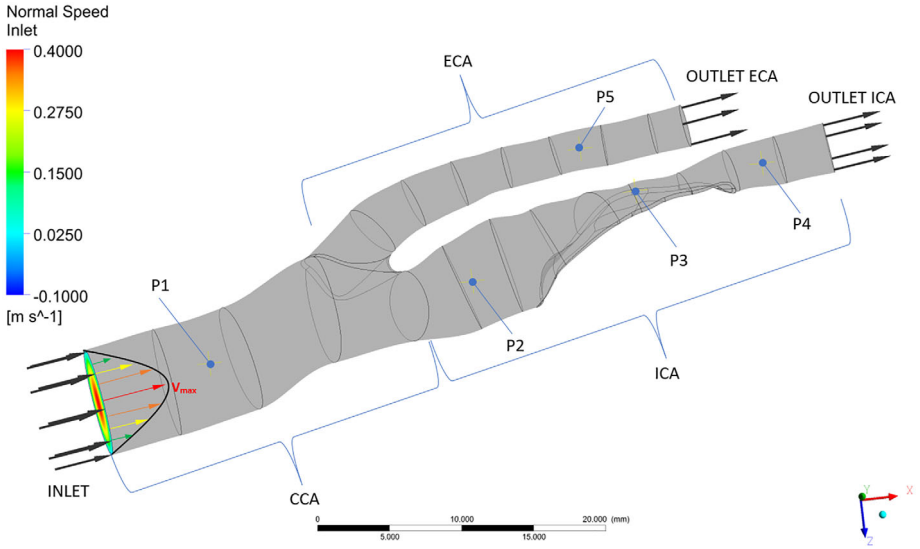

FIGURE 2 Fluid domain with boundary conditions (end-systolic phase) and monitoring points defined in ANSYS CFX Preprocessor

Using a constant value of pressure or zero-pressure condition would not be appropriate since dynamic effects of blood pressure on the compliant wall and the wall response were modeled in this study.

Blood is a non-Newtonian fluid having the shear-thinning rheological behavior that is associated with flattening of erythrocytes and their easier sliding over each other when they are deformed in the high shear strain environment. Numerous mathematical models describing the non-Newtonian nature of blood have been developed.[22,23] However, some authors argue that in large arteries high values of velocity gradients are achieved, thus, blood viscosity becomes constant and the Newtonian model can be employed. Therefore, in this study, the comparison of the results obtained for two Newtonian models and one non-Newtonian model was done. For Newtonian models, two values of dynamic blood viscosity, equal to 3.1 and 3.45 mPa·s, were used. The non-Newtonian model was developed by Jozwik and Obidowski for modeling vertebral blood flows[24] and employed in another study of blood circulation through the circle of Willis.[13] Within this model dynamic viscosity decreases to achieve the constant value equal to 3.45 mPa·s when shear strain rate is higher than 327 s^{-1} (see Equation 1). In all of the presented cases, blood density was assumed to be equal to 1040 kg/m^3. Heat transfer was neglected and no slip conditions were considered at the walls.

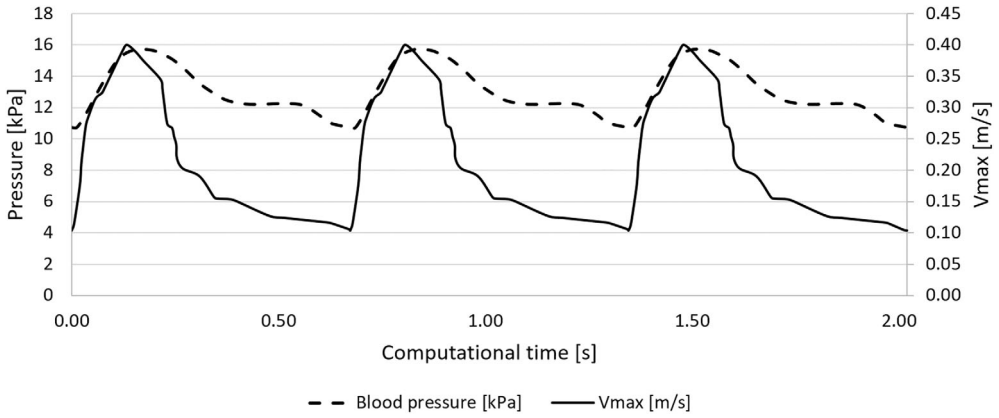

FIGURE 3 V_{max} (in vivo measurements) and normal blood pressure[19] functions used to define boundary conditions, respectively, at the inlet and outlets

$$\begin{cases} \mu = 0.554712 \; for \; \dfrac{\partial v}{\partial y} < 1e^{-9} \\ \mu = \mu_0 \left(\frac{\partial v}{\partial y}\right)^{n-1} for \; 1e^{-9} \le \dfrac{\partial v}{\partial y} < 327 \\ \mu = 0.00345 \; for \; \dfrac{\partial v}{\partial y} \ge 327 \end{cases} \tag{1}$$

Mesh independence tests, a comparison of the results obtained for Newtonian and non-Newtonian blood rheological models, and a timestep assessment were based on rigid-wall steady-state simulations conducted for the peak systolic conditions, for which the monitored hemodynamic parameters can reach the highest values within the cardiac cycle.

Three linear isotropic material models for walls, defined by different values of Young's modulus equal to $E = 0.5$ MPa, $E = 1$ MPa, and $E = 3$ MPa, were arbitrarily chosen to clearly show how significantly the level of compliance affects the hemodynamic parameters monitored in the fluid domain in FSI simulations. As the selected models correspond to other numerical studies of arterial flows,[19–21,25–27] the obtained findings represent the wide range of the possible response of wall and may capture all discrepancies which can occur in different studies. Despite the fact that numerous nonlinear and/or multi-layered material models of arterial wall have been developed[28,29] and even have been successfully employed in numerical modeling of arterial deformation under physiological conditions[18,30] or stenting,[31] they are computationally demanding. However, according to some researchers, the linear material model can be employed in the modeling of the mechanical response of the vascular bed due to the relatively small deformation of arterial walls within the cardiac cycle. Corpataux et al measured the change in the radial artery diameter, which oscillated in the range $\pm 0.67\%$ of the mean diameter.[32] Deformation of carotid artery has been estimated to be larger but it does not exceed $\pm 6\%$ of the mean diameter.[33,34] Additionally, the advantage of the linear model is the relatively short calculation time of simulations providing results that are in good agreement with the data obtained in vivo.[19,35] In all simulations, the Poisson's ratio was assumed to be equal to 0.45. The same value of the ratio was used in other FSI studies on blood flows presented in.[19,20,27,35,36] As the mass matrix is built within structural calculations, the arterial wall was assumed to be an isotropic and one-layered structure with density equal to 1060 kg/m^3.

To stabilize the model in space it was assumed to be fixed in the inlet and outlet cross-sections but also at the inner part of the plaque which was calcified. Thus, the plaque was much stiffer than the arterial wall.[37] The compliant reaction of tissues surrounding the carotid branch was represented by FS that can be understood as numerous small springs connected to external walls of the model. To analyze the influence of LCT on hemodynamics, the set of FSI simulations were carried out for various values of FS (FS = 0 that means no response, FS = 0.05 N/mm^3, FS = 0.1 N/mm^3, FS = 0.2 N/mm^3). The obtained results were compared to those obtained with rigid-wall approach. The Rayleigh damping model was adopted in this study. Selected values of coefficients $\alpha = \beta$ (in the range 0.0001–0.1) were used, however, the influence of damping on the hemodynamic parameters was not observed. All of the presented results were obtained for $\alpha = \beta = 0.01$.

2.3 | Mesh and GCI

All the presented stationary and non-stationary simulations were carried out with the use of the unstructured hybrid tetrahedral grid generated in the fluid domain. The mesh was selected in the mesh independence test based on the grid convergence index (GCI) that was shown in[38] and successfully employed in other numerical studies of blood flows.[39,40] Following the GCI procedure, three meshes containing N_1, N_2, and N_3 finite volumes ($N_1 > N_2 > N_3$) were generated and tested with a rigid-wall approach for peak systolic conditions. To carry out sensitive flow analyses, on the base of the earlier experience, the mesh generation was started from highly precise mesh containing 20 sublayers (N_1) built in the inflation near-wall layer. Then, the mesh density was reduced by slightly diminishing the max. Volume size and lowering the number of inflation sublayers to 10 and 5, respectively, for N_2 and N_3. Then, the representative cell size h was calculated as

$$h = \left[\frac{1}{N}\sum_{i=1}^{N}(\Delta V_i)\right]^{1/3} \tag{2}$$

where N, total number of finite volumes; ΔV_i, volume of the ith cell.

Then, as the grid refinement factor r is expressed by

$$r = \frac{h_{\text{coarse}}}{h_{\text{fine}}} \tag{3}$$

and the relation $h_1 < h_2 < h_3$ was assumed, refinement factors could be found from: $r_{21} = h_2/h_1$ and $r_{32} = h_3/h_2$. As advised in Reference 38, the refinement factor r should be higher than 1.3. In the next step, differences between the selected parameters ϕ obtained in simulations performed for sequent meshes, expressed by $\varepsilon_{21} = \phi_2 - \phi_1$ and $\varepsilon_{32} = \phi_3 - \phi_2$, were calculated. In this study, ϕ is represented by three area-averaged parameters insensitive to local mesh imperfections: area-averaged WSS (AAWSS) on the wall, velocity, and mass flow rate averaged over the ICA inlet and ECA outlet cross-sections. Then, the apparent order p was found using equations

$$p = \frac{1}{\ln(r_{21})}\left|ln\left|\frac{\varepsilon_{32}}{\varepsilon_{21}}\right| + q(p)\right| \tag{4}$$

$$q(p) = ln\left(\frac{r_{21}^p - s}{r_{32}^p - s}\right) \tag{5}$$

$$s = sgn\left(\frac{\varepsilon_{32}}{\varepsilon_{21}}\right) \tag{6}$$

where the functions representing p and $q(p)$ must be found iteratively. Then, extrapolated values of the investigated parameters were calculated as follows

$$\phi_{ext}^{21} = \frac{r_{21}^p \phi_1 - \phi_2}{r_{21}^p - 1} \tag{7}$$

Furthermore, the approximate relative error and extrapolated relative error were calculated

$$e_a^{21} = \left|\frac{\phi_1 - \phi_2}{\phi_1}\right| \tag{8}$$

$$e_{\text{ext}}^{21} = \left|\frac{\phi_{\text{ext}}^{21} - \phi_1}{\phi_{\text{ext}}^{21}}\right| \tag{9}$$

TABLE 1 Parameters and results obtained in the mesh independence test based on the grid convergence index method

Parameter	Φ = AAWSS [Pa]			Φ = area-averaged velocity [m/s]		Φ = area-averaged mass flow [kg/m^3]	
Localization	Wall	Plaque inner	Plaque outer	ECA out	ICA out	ECA out	ICA out
$N_1;N_2;N_3$	15,333,243; 1,860,627; 375,513						
r_{21}	2.02						
r_{32}	1.07						
Φ_1	4.87	11.77	7.15	0.7592	0.38856	0.005694	0.003594
Φ_2	4.42	10.90	6.85	0.7622	0.38860	0.005707	0.003583
Φ_3	3.41	8.76	6.00	0.7756	0.39020	0.005783	0.003513
p	1.82	1.95	2.17	2.99	6.91	3.46	3.61
$\Phi^{32}{}_{ext}$	5.04	12.07	7.24	0.76	0.39	0.0057	0.0036
$e^{32}{}_{a}$ [%]	22.93	19.62	12.36	1.76	0.41	1.33	1.95
$e^{32}{}_{ext}$ [%]	12.27	9.68	5.37	0.45	0.01	0.25	0.33
$GCI^{32}{}_{coarse}$ [%]	17.48	13.40	7.09	0.56	0.01	0.31	0.42
$\Phi^{21}{}_{ext}$	5.04	12.07	7.24	0.76	0.39	0.006	0.004
$e^{21}{}_{a}$ [%]	9.17	7.41	4.24	0.39	0.011	0.228	0.31
$e^{21}{}_{ext}$ [%]	3.41	2.46	1.17	0.06	0.0001	0.02	0.03
$\mathbf{GCI^{21}_{fine}}$ [%]	**4.42**	**3.15**	**1.48**	**0.07**	**0.0001**	**0.0275**	**0.0328**

Finally, the fine-grid convergence index GCI was calculated from

$$\mathrm{GCI}^{21}_{\mathrm{fine}} = \frac{1.25\mathrm{e}^{21}_{a}}{r^{p}_{21} - 1} \tag{10}$$

The results obtained within GCI testing are presented in Table 1. As the $\mathrm{GCI}_{\mathrm{fine}}$ was lower than 5% for all investigated parameters ϕ, the mesh N_2 was assessed to be fine enough for further calculations. This mesh provides a sufficient compromise between precision and the total time of calculations. The chosen mesh (Figure 4) is characterized by the following metrics: number of finite volumes = 1,860,627, number of nodes = 608,287, max. Volume size = 0.2 mm, averaged Skewness = 0.226, averaged element quality = 0.688. The mesh representing the walls (Figure 4), consisting of 146,221 elements, was significantly coarser than the fluid one (av. Skewness = 0.312) as structural computing is much more time-demanding than fluid flow calculations.[36]

2.4 | Theory and calculations

As the transient FSI modeling requires both, fluid and structural analyses to be done simultaneously, a two-way coupled technique involving ANSYS CFX and Transient Structural modules was employed.

2.4.1 | Governing equations

The modeled transient blood flow was assumed to be incompressible and thermal effects associated with heat conductivity and energy dissipation were not considered. Moreover, the sum of body forces is neglected as the motionless patient was examined in the supine position, thus, the Unsteady Reynolds Averaged Navier–Stokes (URANS) equations governing the fluid motion solved by CFX[41] were simplified to

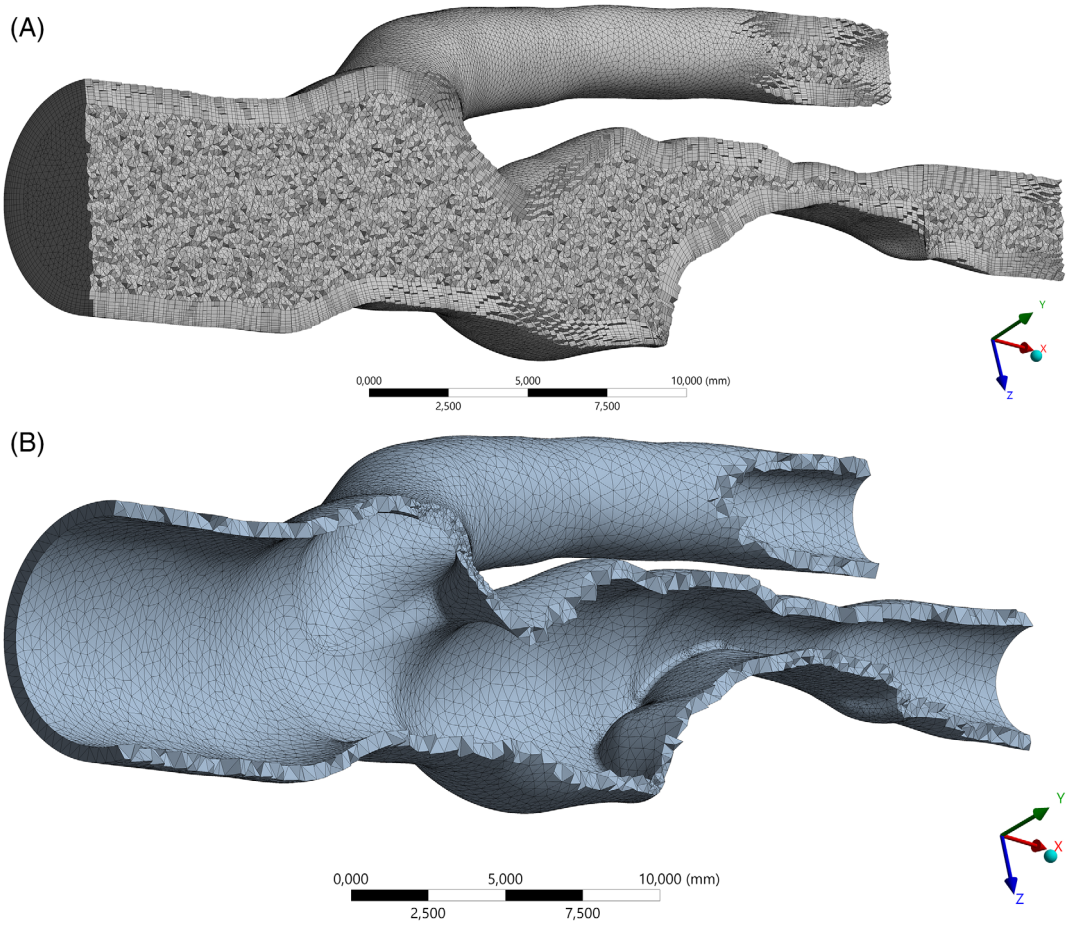

FIGURE 4 Longitudinal cross-sections of mesh in fluid domain (1,860,627 finite volumes) and structural domain representing the wall (146,221 elements) generated in ANSYS

$$\frac{\partial U_j}{\partial x_j} = 0 \tag{11}$$

$$\rho\left(\frac{\partial U_i}{\partial t} + \frac{\partial}{\partial x_j}\left(U_i U_j\right)\right) = -\frac{\partial p}{\partial x_i} + \frac{\partial}{\partial x_j}\left(\tau_{ij} - \rho\overline{u_i u_j}\right) \tag{12}$$

where ρ—constant blood density equal to 1040 kg/m^3, p—pressure, τ—stress tensor (including normal and shear components), $\rho\overline{u_i u_j}$ —Reynolds (turbulent) stresses related to turbulent fluxes, and U_i and U_j—velocity components, which can be divided into an average and fluctuating time-varying components calculated as follows

$$U_i = \overline{U_i} + u_i \tag{13}$$

where u_i is a varying component and U_i is an averaged component that can be expressed as

$$\overline{U_i} = \frac{1}{\Delta t}\int_t^{t+\Delta t} U_i dt \tag{14}$$

To close URANS equations, in which the Reynolds stresses are unknown, additional formulas were considered. These complementary expressions are called the statistical model of turbulence. Despite the fact that the blood flow in the CCA was assumed to be laminar, it can undergo disturbances in the carotid bifurcation and stenosis. Thus, the shear

stress transport (SST) turbulence model was chosen. The SST approach connects advantages of k-ε that is widely accepted for modeling of the free stream flow and *k-ω* describing the near-wall treatment for low-Reynolds number flows by assuming the relation between turbulence viscosity with turbulence kinetic energy and turbulent frequency. Therefore, as WSS is an important hemodynamic parameter deeply investigated in this study, the SST model allowing one to achieve the desirable convergence level for low values of the Reynolds number was chosen.[41,42]

The results obtained by the steady-state simulation carried out with a convergence residual target equal to 10^{-6} and a high-resolution scheme, were utilized as initial conditions for transient flow simulations for rigid- and compliant-wall approaches. Transient computations were supported by high resolution and second-order backward Euler schemes. On the basis of our previous experience and similarly to,[19] stability and the desired convergence level of FSI simulations were achieved by means of the mass flux pressure coefficient defining the source at the interface. Additionally, the range of 1 to 8 coefficient loops was set to control convergence.

Three values of timestep (dt = 0.01 s, dt = 0.001 s, dt = 0.0005 s) were tested with the rigid-wall approach, however, it was observed that dt influenced only on the local Courant number without significant affection on the investigated hemodynamic parameters, thus the value equal to 0.01 s was chosen to conduct highly time-consuming FSI simulations.

Another package of equations was solved by Transient Structural on the other side of the fluid–solid interface to model the mechanical response of the wall structure for a load of changing pressure in the fluid domain. According to[43] the basic equation of motion solved by ANSYS Mechanical is as follows

$$\{F(t)\} = [M]\{\ddot{u}\} + [C]\{\dot{u}\} + [K]\{u\} \tag{15}$$

where $\{F(t)\}$—load vector (coming from pressure in the fluid domain), $[M]$—mass matrix, $[C]$—damping matrix, $[K]$—stiffness matrix, $\{\ddot{u}\}$—nodal acceleration vector, $\{\dot{u}\}$—nodal velocity vector, $\{u\}$—nodal displacement vector. Therefore, $[M]\{\ddot{u}\}$, $[C]\{\dot{u}\}$, and $[K]\{u\}$ represent, respectively, inertia forces, damping forces, and internal forces. To solve Equation (15) ANSYS Mechanical uses the Newmark time-integration method and an improved implicit technique called the Hilber-Hughes-Taylor method allowing for energy dissipation.

2.4.2 | Fluid–structure coupling

As two-way FSI analyses were carried out, the automatic System Coupling module available in ANSYS Workbench 2020 R1 was used to combine calculations performed in CFX and Transient Structural modules. The coupling uses the staggered approach and allows the forces, coming from the pressure and stresses determined in the fluid domain, to be transferred across the fluid–solid interface. Then, displacements, stresses, and strain in the solid structure are computed and the information comes back to the fluid side. Therefore, the physics can be parallelly solved in both domains until convergence is attained by the System Coupling.[44,45] The same range of coupling iterations was set for all the FSI simulations to achieve convergence in the optimal time of 43–56 h, which is roughly 10 times longer than for rigid-wall cases. A single workstation was used for all calculations: Intel Core i7-3930K CPU 3.20 GHz 6 cores Hyper-V, RAM DIMM 1600 MHz 64 GB.

3 | RESULTS

The hemodynamic parameters were monitored at five points located in the fluid domain shown in Figure 2 or were determined at the zones defined on the outer surfaces of that domain as depicted in Figure 5. To show the significance of the compliant-wall approach and to compare the results attained in FSI simulations for a range of Young's modulus, foundation stiffness, or damping coefficients, time-averaged parameters were extracted from the transient results obtained in the third cardiac cycle. Changes in selected parameters were presented over time.

Besides blood velocity and pressure, other metrics characterizing hemodynamics investigated here are:

- wall shear stress (absolute value) calculated as

$$WSS = \tau_\omega = \rho u^* u_\tau \tag{16}$$

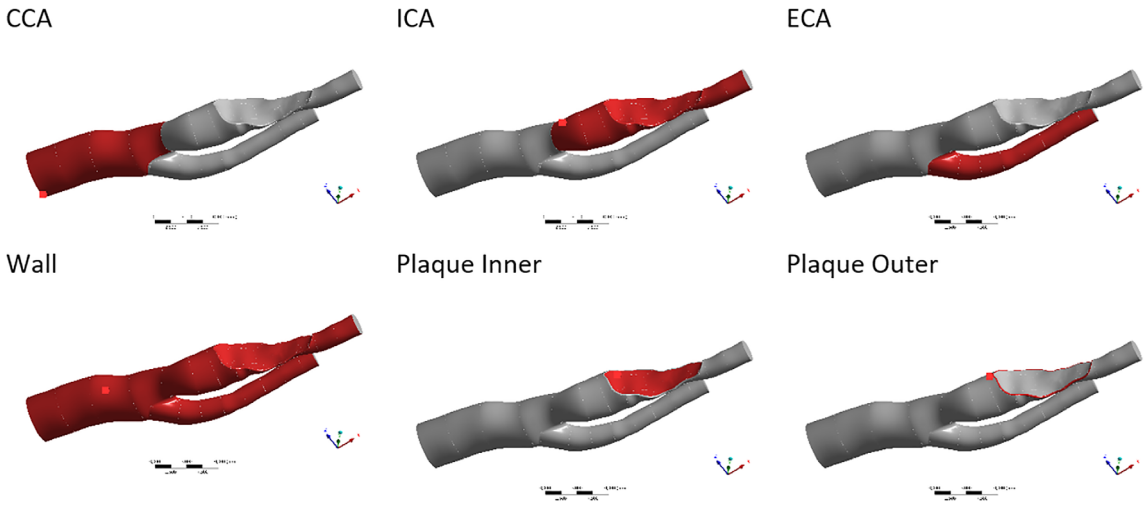

FIGURE 5 Zones specified on the outer surfaces of the fluid domain in Ansys Mesher

where u^*—near-wall velocity and u_τ—friction velocity are calculated from Scalable Wall Function developed by ANSYS CFX, which is based on the empirical formulas describing the logarithmic change of the velocity near the wall when velocity at the nearest point from the wall is determined[41];

- shear strain rate determining the blood viscosity defined by

$$sstrnr = \left[2\frac{\partial U_i}{\partial x_j}S_{ij}\right]^{\frac{1}{2}} \tag{17}$$

where

$$S_{ij} = \frac{1}{2}\left(\frac{\partial U_i}{\partial x_j} + \frac{\partial U_j}{\partial x_i}\right) \tag{18}$$

- vorticity magnitude expressed as

$$\Omega = \sqrt{2\Omega_{ij}\Omega_{ij}} \tag{19}$$

where Ω_{ij} is the vorticity tensor

$$\Omega_{ij} = \frac{1}{2}\left(\frac{\partial U_i}{\partial x_j} - \frac{\partial U_j}{\partial x_i}\right) \tag{20}$$

3.1 | Newtonian versus non-Newtonian rheological models

To compare blood rheological models, relatively less time-consuming stationary simulations with a rigid-wall approach were performed for the peak-systolic conditions. A comparison of the results obtained for two selected Newtonian and the non-Newtonian rheological models did not show significant influence of the chosen models on hemodynamic parameters (Figure 6). However, noticeable discrepancies in vorticity and shear strain were found at the monitoring points P2 (ICA) and P3 (stenosis). The significant difference in vorticity and shear strain in P3 if compared to the other points is associated with huge acceleration of blood flow in the stenotic zone and local

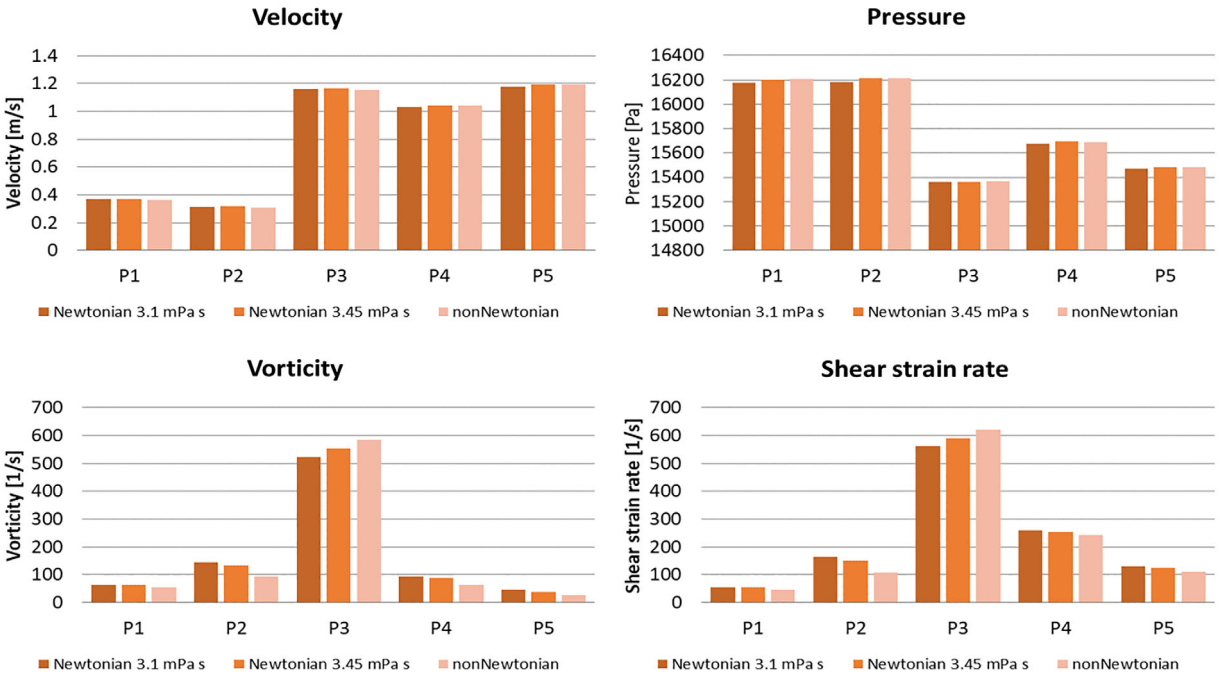

FIGURE 6 Comparison of parameters obtained at the monitoring points in steady-state simulations at the peak-systolic point for selected rheological models (rigid-wall approach)

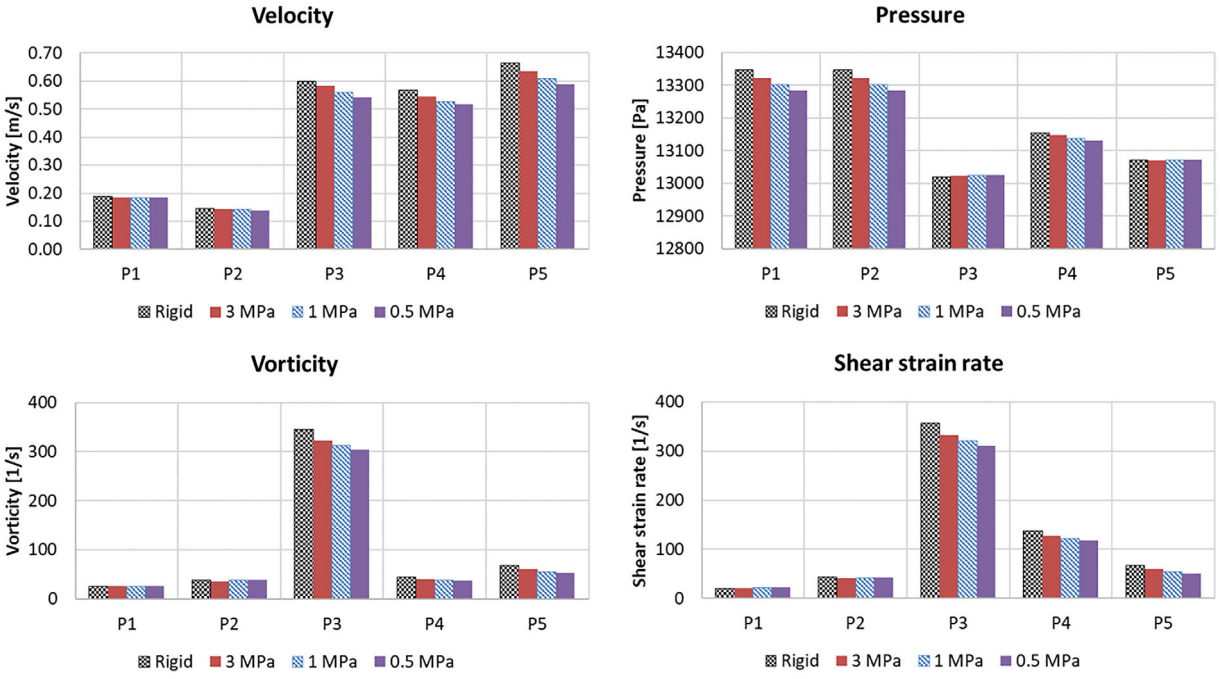

FIGURE 7 Comparison of time-averaged parameters obtained at the monitoring points in transient simulations carried out with rigid-wall and fluid structure interaction approaches for selected values of Young's modulus. $E = 3$ MPa, $E = 1$ MPa, and $E = 0.5$ MPa (FS $= 0.1$ N/mm^3).

complexity of flow patterns. Therefore, due to the fact that three-dimensional flow was further modeled and similar differences can occur in undefined points or zones, it was decided to use the non-Newtonian model in FSI simulations.

3.2 | Elasticity-related wall-compliance

Figure 7 presents a comparison of time-averaged hemodynamic parameters obtained in the monitoring points for rigid- and compliant-wall approaches. To carry out FSI simulations, three values of Young's modulus were used (with FS = 0.1 N/mm^3). It is clearly visible that almost in all cases the results are overestimated in rigid-wall simulations. As expected, the highest differences can be found between rigid-wall and the most flexible model ($E = 0.5$ MPa). In point P5 the discrepancies reach even 23.8%, 21.9%, and 11.4%, respectively, for time-averaged shear strain, vorticity, and velocity. Differences in pressure are relatively low and they are higher if monitored closer to the inlet (0.47% in P1). It is

TABLE 2 Comparison of peak-systolic parameters obtained in particular zones in transient simulations carried out with rigid-wall and FSI approaches for selected values of Young's modulus: $E = 3$ MPa, $E = 1$ MPa, and $E = 0.5$ MPa (FS = 0.1 N/mm^3)

		Compliant					
Peak-systolic parameters ($t = 1.48$ s)	**Rigid**	**3 MPa**	**Compliant /rigid [%]**	**1 MPa**	**Compliant /rigid [%]**	**0.5 MPa**	**Compliant /rigid [%]**
Max WSS Wall [Pa]	47.654	43.564	**8.58**	41.024	**13.91**	39.461	**17.19**
AAWSS Wall [Pa]	4.507	4.164	**7.62**	3.897	**13.52**	3.737	**17.08**
AAWSS Plaque Inner [Pa]	10.929	10.162	**7.02**	9.561	**12.52**	9.196	**15.86**
AAWSS Plaque Outer [Pa]	6.962	6.662	**4.31**	6.374	**8.44**	6.187	**11.13**
Flow rate ECA Outlet [cm^3/s]	5.470	5.298	**3.15**	5.231	**4.38**	5.215	**4.66**
Flow rate ICA Outlet [cm^3/s]	3.444	3.503	**−1.70**	3.484	**−1.14**	3.483	**−1.12**
Max Y plus	1.381	1.321	**4.38**	1.263	**8.54**	1.220	**11.67**
Area-Averaged Velocity ECA Outlet [m/s]	0.760	0.736	**3.14**	0.726	**4.42**	0.724	**4.76**
Area-Averaged Velocity ICA Outlet [m/s]	0.381	0.381	**0.03**	0.376	**1.32**	0.373	**2.15**
Area-Averaged pressure Inlet [Pa]	16,334	16,259	**0.46**	16,193	**0.86**	16,161	**1.06**

Note: Bold indicates the difference in values between the compliant and the rigid case.
Abbreviations: AAWSS, area-averaged wall shear stress; FSI, fluid structure interaction; WSS, wall shear stress.

TABLE 3 Comparison of end-diastolic parameters obtained in particular zones in transient simulations carried out with rigid-wall and FSI approaches for selected values of Young's modulus: $E = 3$ MPa, $E = 1$ MPa, and $E = 0.5$ MPa (FS = 0.1 N/mm^3)

		Compliant					
End-diastolic parameters ($t = 2.02$ s)	**Rigid**	**3 MPa**	**Compliant /rigid [%]**	**1 MPa**	**Compliant /rigid [%]**	**0.5 MPa**	**Compliant /rigid [%]**
max WSS Wall [Pa]	7.579	7.284	**3.90**	7.000	**7.64**	6.779	**10.56**
AAWSS Wall [Pa]	0.950	0.923	**2.89**	0.896	**5.68**	0.876	**7.81**
AAWSS Plaque Inner [Pa]	2.058	2.0063	**2.53**	1.951	**5.24**	1.903	**7.54**
AAWSS Plaque Outer [Pa]	0.959	0.965	**−0.57**	0.955	**0.42**	0.940	**1.97**
Flow rate ECA Outlet [cm^3/s]	1.468	1.462	**0.46**	1.471	**−0.20**	1.480	**−0.79**
Flow rate ICA Outlet [cm^3/s]	0.854	0.886	**−3.72**	0.894	**−4.73**	0.897	**−5.07**
max Y plus	0.570	0.559	**1.90**	0.547	**4.00**	0.537	**5.79**
Area-Averaged Velocity ECA Outlet [m/s]	0.204	0.203	**0.44**	0.204	**−0.20**	0.205	**−0.74**
Area-Averaged Velocity ICA Outlet [m/s]	0.0890	0.0921	**−3.48**	0.0930	**−4.44**	0.0932	**−4.70**
Area-Averaged pressure Inlet [Pa]	10,850	10,845	**0.05**	10,840	**0.09**	10,837	**0.12**

Note: Bold indicates the difference in values between the compliant and the rigid case.
Abbreviations: AAWSS, area-averaged wall shear stress; FSI, fluid structure interaction; WSS, wall shear stress.

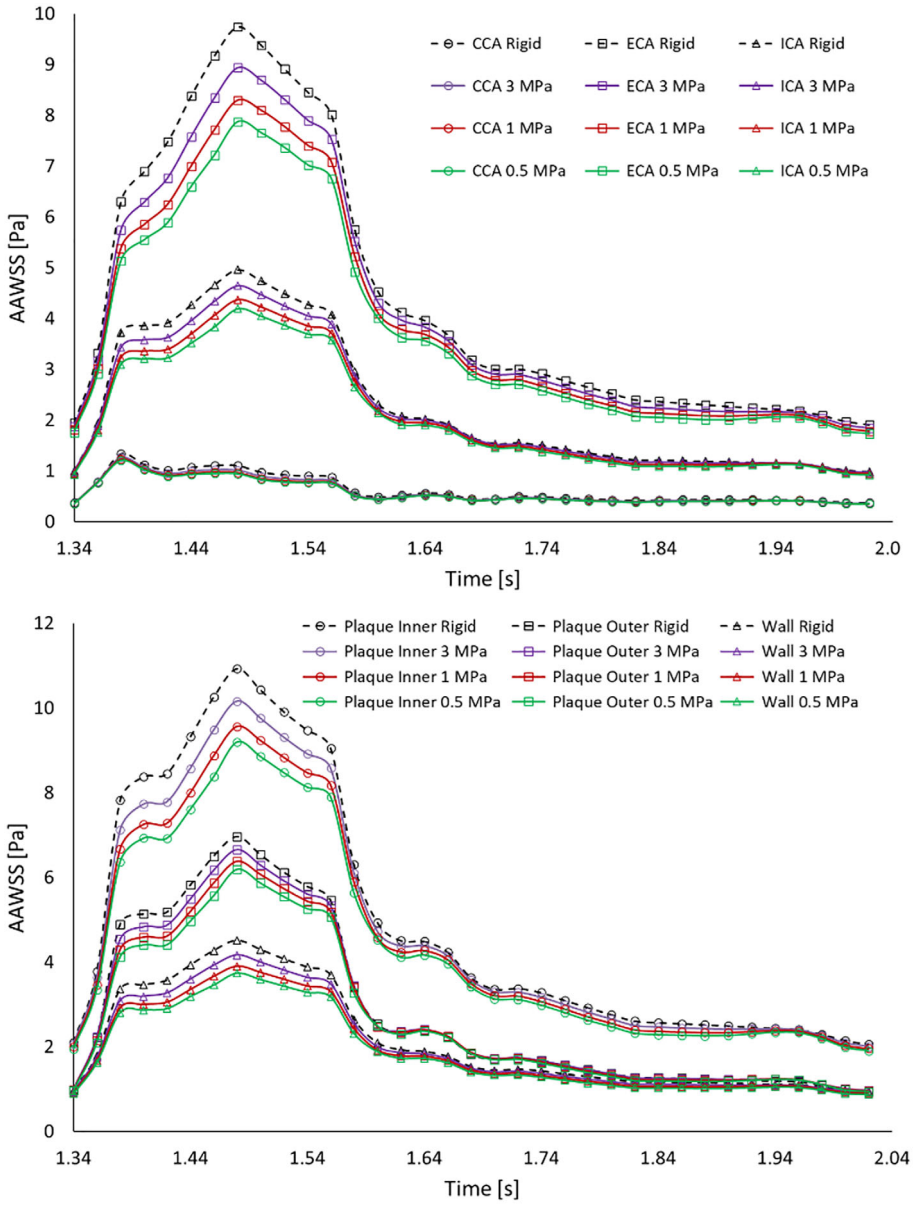

FIGURE 8 Changes of AAWSS obtained at the defined zones in transient simulations carried out with rigid-wall and fluid structure interaction approaches for selected values of Young's modulus: $E = 3$ MPa, $E = 1$ MPa, and $E = 0.5$ MPa (FS = 0.1 N/mm^3)

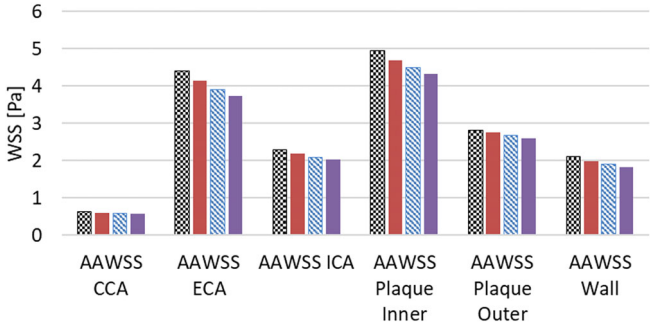

FIGURE 9 Comparison of time-averaged AAWSS obtained at the defined zones in transient simulations carried out with rigid-wall and fluid structure interaction approaches for selected values of Young's modulus. $E = 3$ MPa, $E = 1$ MPa, and $E = 0.5$ MPa (FS = 0.1 N/mm^3)

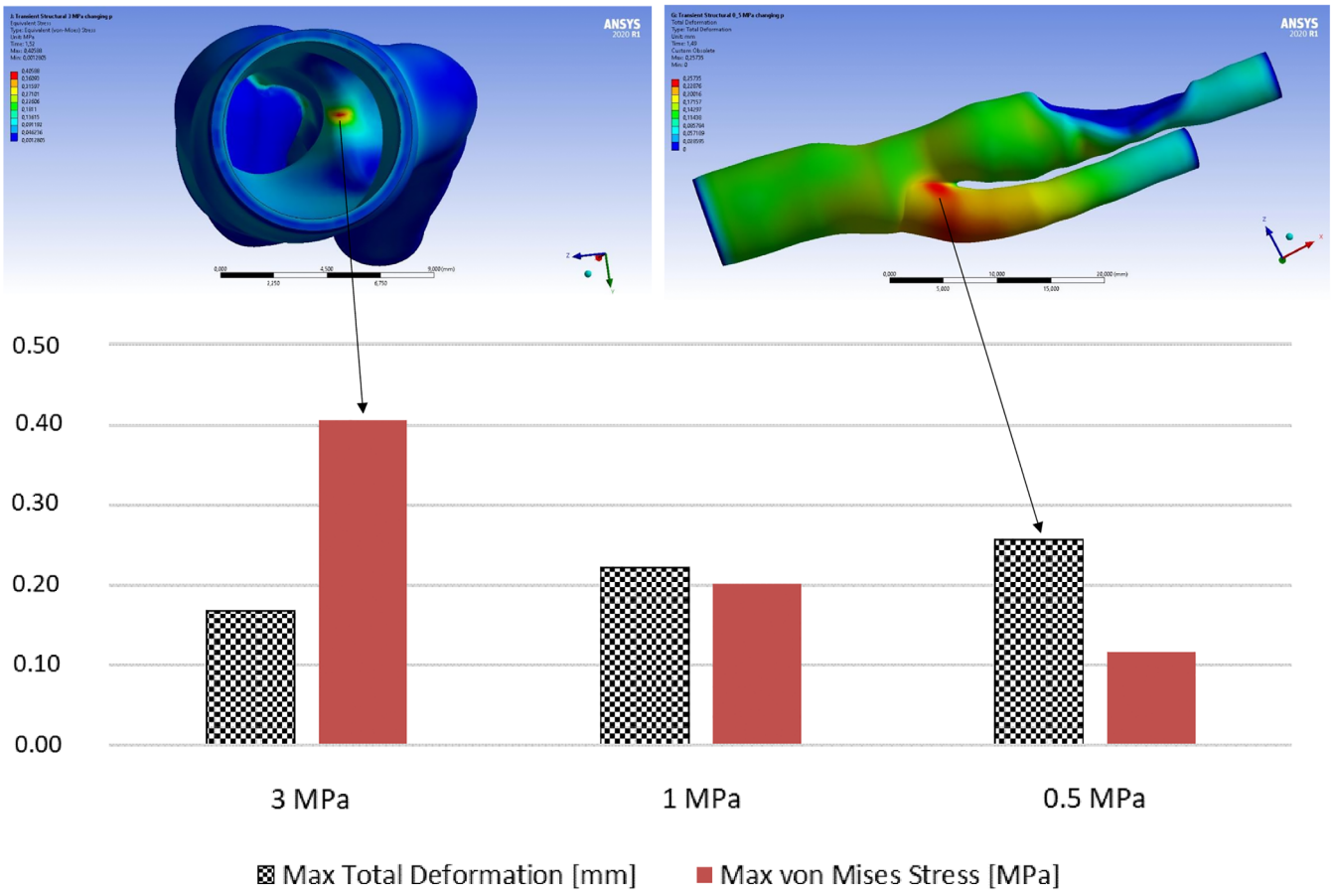

FIGURE 10 Comparison of peak-systolic deformation and stress determined in the structural domain in FSI simulations for selected values of Young's modulus: $E = 3$ MPa, $E = 1$ MPa, and $E = 0.5$ MPa (FS = 0.1 N/mm^3).

worth mentioning that significantly high vorticity and shear strain were found in stenosis in the environment of relatively high velocity and associated low pressure (Venturi effect).

Table 2 shows a comparison of peak-systolic ($t = 1.48$ s) parameters characterizing the blood flow: maximal WSS and AAWSS in selected zones, mass flow rates and area-averaged velocity at the outlet surfaces, and area-averaged pressure determined at the inlet cross-section. An analogous table showing the end-diastolic results ($t = 2.02$ s) is presented in Table 3. The tables give quantitative information about the range in which the parameters change within the cardiac cycle. Additionally, percentage differences of the results obtained for compliant models with a reference to the rigid model are given. The maximal influence of wall flexibility on hemodynamics, as expected, concerns the most compliant model ($E = 0.5$ MPa). In this case, maximal WSS detected in the fluid domain varies within the cardiac cycle between 6.8–39.5 Pa that is 10%–17% lower than for the rigid model (7.6–47.6 Pa). Moreover, if compared to the rigid-wall approach, in this case, a non-negligible difference in flow rate was determined in ECA in peak-systole (4.66%) while the highest difference in flow rate in ICA was found for end-diastole (5.07%).

Changes of AAWSS monitored over time in the particular zones are depicted in Figure 8, whereas time-averaged values of AAWSS were compared in Figure 9. Time-averaged AAWSS on the Wall does not exceed the typical arterial level of 7–10 Pa[7] as the maximal values are concentrated on the stenosis and a part of ECA (see: Figure 15). The differences in time-averaged AAWSS obtained for rigid and the most compliant model ($E = 0.5$ MPa) exceeded 10% in almost all considered zones: CCA (10.11%), ECA (15.38%), ICA (11.81%), Plaque Inner (12.67%), Plaque Outer (8.14%), and the whole Wall (13.23%). Moreover, time-averaged AAWSS is higher in ECA than in ICA that is associated with the flow division and difference in mean area-averaged blood velocity. This parameter is much lower in CCA than in ECA and ICA, which is in good agreement with observations of Lopes et al.[20]

The influence of the selected values of Young's modulus on changes in the maximal/average values of mesh displacement and von Misses stress detected within the third cardiac cycle in the whole structural domain is presented in

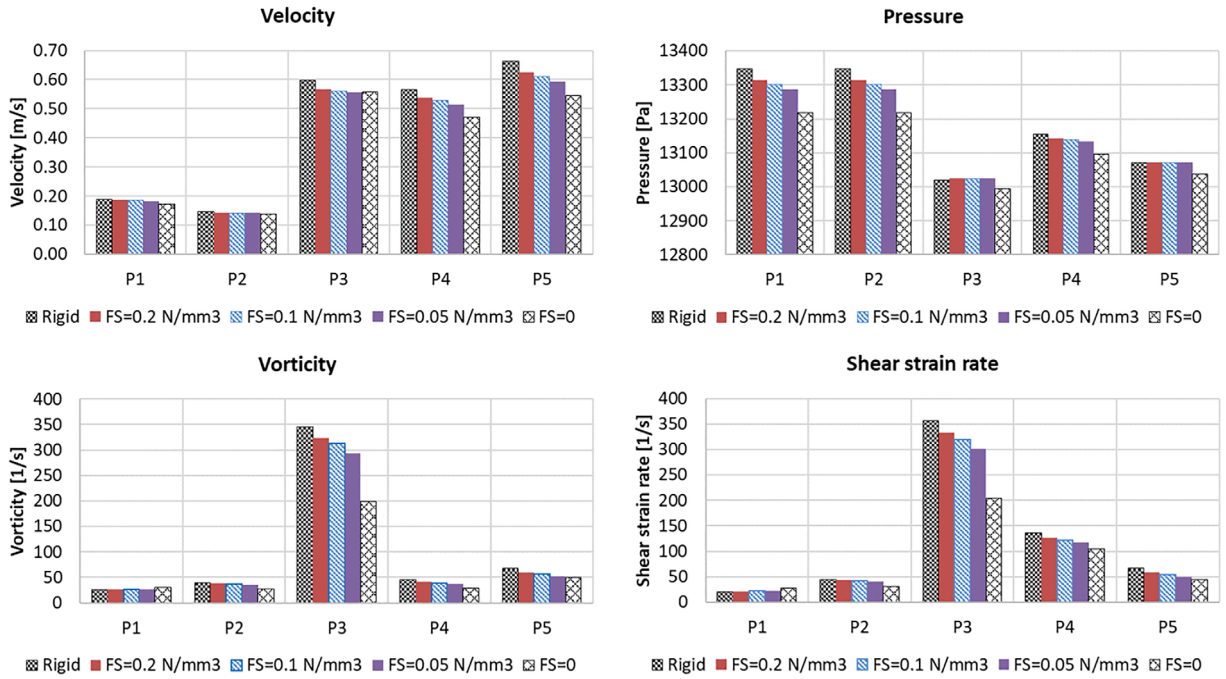

FIGURE 11 Comparison of time-averaged parameters obtained at the monitoring points in transient simulations carried out with rigid-wall and fluid structure interaction approaches for selected values of foundation stiffness: FS = 0.2 N/mm^3, FS = 0.1 N/mm^3, FS = 0.05 N/mm^3, and FS = 0 (E = 1 MPa)

TABLE 4 Comparison of peak-systolic parameters obtained in particular zones in transient simulations carried out with rigid-wall and FSI approaches for selected values of foundation stiffness coefficients: FS = 0.2 N/mm^3, FS = 0.05 N/mm^3, and FS = 0 (E = 1 MPa)

		Compliant					
Peak-systolic parameters (t = 1.48 s)	**Rigid**	**0.2 N/mm^3**	**Compliant/rigid [%]**	**0.05 N/mm^3**	**Compliant/rigid [%]**	**0**	**Compliant/rigid [%]**
max WSS Wall [Pa]	47.654	43.065	**9.63**	38.424	**19.37**	31.853	**33.16**
AAWSS Wall [Pa]	4.507	4.0894	**9.26**	3.681	**18.32**	2.916	**35.29**
AAWSS Plaque Inner [Pa]	10.929	9.956	**8.90**	9.126	**16.50**	7.523	**31.17**
AAWSS Plaque Outer [Pa]	6.962	6.523	**6.30**	6.225	**10.59**	5.645	**18.91**
Flow rate ECA Outlet [cm^3/s]	5.470	5.340	**2.37**	5.070	**7.31**	4.277	**21.81**
Flow rate ICA Outlet [cm^3/s]	3.444	3.454	**−0.28**	3.537	**−2.68**	3.619	**−5.08**
max Y plus	1.381	1.299	**5.97**	1.222	**11.51**	1.076	**22.07**
Area-Averaged Velocity ECA Outlet [m/s]	0.760	0.742	**2.41**	0.704	**7.36**	0.594	**21.86**
Area-Averaged Velocity ICA Outlet [m/s]	0.381	0.376	**1.40**	0.378	**0.79**	0.378	**0.63**
Area-Averaged pressure Inlet [Pa]	16,334	16,235	**0.61**	16,150	**1.13**	16,017	**1.94**

Note: Bold indicates the difference in values between the compliant and the rigid case.
Abbreviations: AAWSS, area-averaged wall shear stress; FSI, fluid structure interaction; WSS, wall shear stress.

Appendix **S1**. A comparison of maximal displacement and maximal stress vs. Young's modulus is depicted in Figure 10. The maximal displacement equal to 0.2573 mm was found in ECA in the area of the carotid bifurcation for E = 0.5 MPa at t = 1.49 s (Figure 10). The maximal von Mises stress (0.1158 MPa) and maximal equivalent

TABLE 5 Comparison of end-diastolic parameters obtained in particular zones in transient simulations carried out with rigid-wall and FSI approaches for selected values of foundation stiffness: FS = 0.2 N/mm^3, FS = 0.05 N/mm^3, and FS = 0 (E = 1 MPa)

		Compliant					
End-diastolic parameters (t = 2.02 s)	**Rigid**	**0.2 N/mm^3**	**Compliant/rigid [%]**	**0.05 N/mm^3**	**Compliant/rigid [%]**	**0**	**Compliant/rigid [%]**
max WSS Wall [Pa]	7.579	7.156	**5.59**	6.880	**9.23**	6.764	**10.75**
AAWSS Wall [Pa]	0.950	0.913	**3.89**	0.878	**7.64**	0.825	**13.21**
AAWSS Plaque Inner [Pa]	2.058	1.979	**3.88**	1.923	**6.57**	1.848	**10.25**
AAWSS Plaque Outer [Pa]	0.959	0.951	**0.82**	0.964	**−0.55**	1.027	**−7.11**
Flow rate ECA Outlet [cm^3/s]	1.468	1.474	**−0.39**	1.462	**0.46**	1.420	**3.27**
Flow rate ICA Outlet [cm^3/s]	0.854	0.875	**−2.48**	0.925	**−8.33**	1.065	**−24.77**
max Y plus	0.570	0.552	**3.02**	0.541	**4.99**	0.525	**7.74**
Area-Averaged Velocity ECA Outlet [m/s]	0.204	0.205	**−0.39**	0.203	**0.44**	0.197	**3.24**
Area-Averaged Velocity ICA Outlet [m/s]	0.0890	0.0910	**−2.17**	0.0961	**−7.99**	0.1110	**−24.67**
Area-Averaged pressure Inlet [Pa]	10,850	10,843	**0.06**	10,837	**0.12**	10,831	**0.18**

Note: Bold indicates the difference in values between the compliant and the rigid case.
Abbreviations: AAWSS, area-averaged wall shear stress; FSI, fluid structure interaction; WSS, wall shear stress.

elastic strain (0.2318 mm/mm) in this case were found on the inner side of the structural domain in the branching zone at t = 2.52 s. As expected, for the least elastic case with E = 3 MPa, the maximal deformation was much lower (0.1668 mm), however, maximal von Mises stress equal to 0.4059 MPa (Figure 10) and equivalent elastic strain (0.0912 mm/mm) were achieved in the same regions at the same moments superimposing maximal blood pressure exerted on the wall.

3.3 | Foundation-related LCT-compliance

Another set of FSI simulations was performed to investigate the influence of compliance of LCT surrounding the carotid bifurcation. These simulations were carried out using different values of FS (for E = 1 MPa). As expected, the unsupported external wall of the structural domain (FS = 0), as the most compliant, is responsible for the most significant differences in hemodynamics when compared to the rigid-wall approach.

Figure 11 shows a comparison of the time-averaged flow parameters monitored in points P1-P5 in relation to the values determined in the rigid-wall case. Similarly to previous comparisons, the highly compliant unsupported wall usually results in significant decrease of the parameters obtained in the set. The differences are extremely high for vorticity and shear strain determined in P3 where the parameters achieve elevated levels (respectively 42.47% and 42.75% for FS = 0 vs. rigid wall). The influence of FS on the peak-systolic parameters obtained in the defined zones is presented in Table 4, where percentage differences be-tween compliant-wall and rigid-wall approaches are given. End-diastolic data are given in Table 5. High compliance, achieved for FS = 0, gives significantly lower AAWSS determined on the whole wall within the cardiac cycle (13.21%–35.29% if compared to the rigid case). Moreover, the wall-foundation strongly affects flow rate and, consequently, the area-averaged velocity at the outlet surfaces that can exceed 20% of the reference value obtained for rigid-wall approach.

Changes of AAWSS monitored over time in the particular zones are depicted in Figure 12, whereas the time-averaged values of AAWSS were compared in Figure 13. Similarly to the observations presented in section 4.2, time-averaged AAWSS remains at the arterial level as the highest values of this parameter consider the same reference rigid-wall simulation. However, the differences in time-averaged AAWSS obtained in the defined zones for rigid and the most resilient model (FS = 0) are much higher in this set and exceed even 25%: CCA (28.24%), ECA (25.72%), ICA

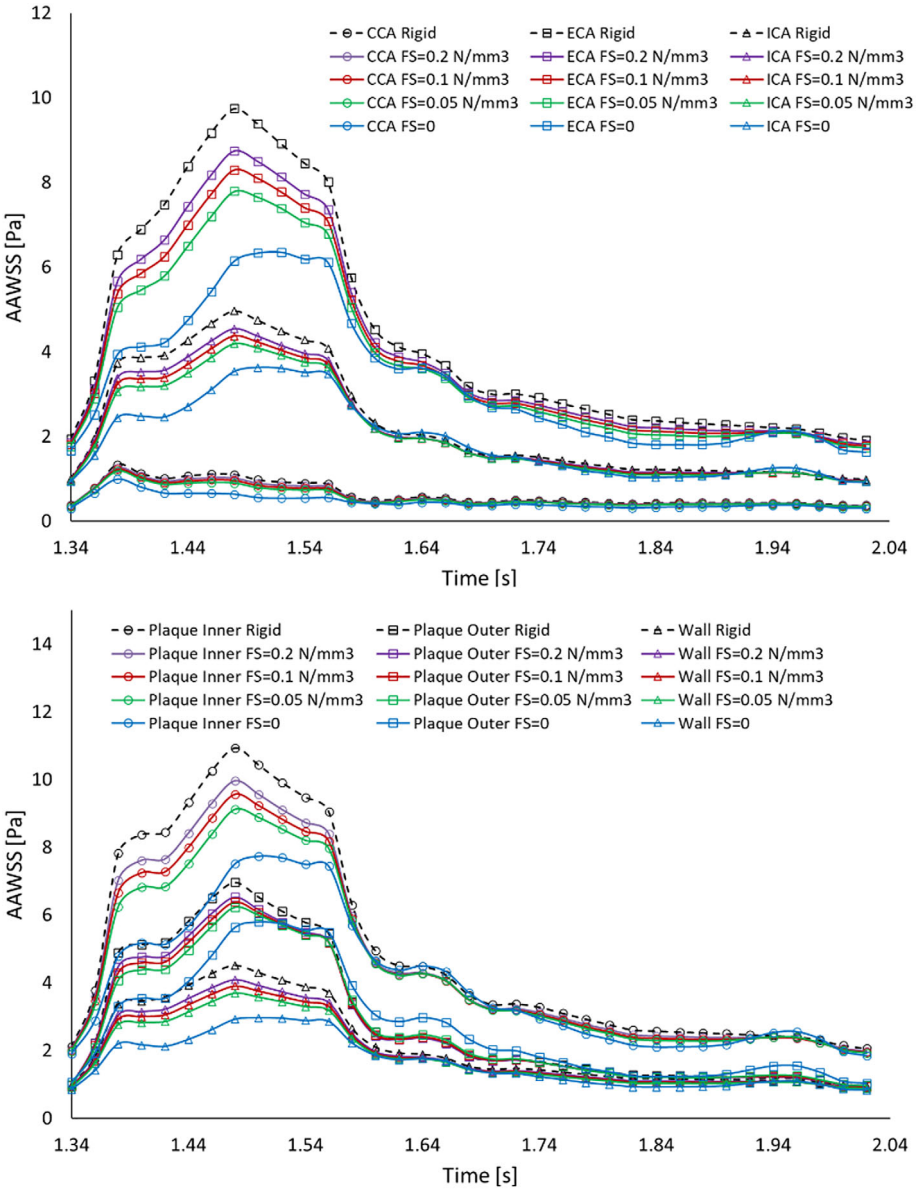

FIGURE 12 Changes of AAWSS obtained at the defined zones in transient simulations carried out with rigid-wall and fluid structure interaction approaches for selected values of foundation stiffness: FS = 0.2 N/mm^3, FS = 0.1 N/mm^3, FS = 0.05 N/mm^3, and FS = 0 (E = 1 MPa)

(17.25%), Plaque Inner (20.16%), Plaque Outer (5.78%), and the whole Wall (23.69%). The trend is similar as in the previous set and time-averaged AAWSS is much lower in relatively broad CCA than in ECA and ICA, which is related to similar flow division in the carotid branch.

The influence of FS on changes vs. time in the maximal/average values of mesh displacement and von Misses stress detected in the whole structural domain is shown in Appendix S1. The comparison of maximal displacement and maximal stress obtained for the selected values of FS is depicted in Figure 14. In this set, the maximal displacement (1.2119 mm), maximal von Mises stress (0.7691 MPa), and maximal equivalent elastic strain (0.7705 mm/mm) were found in the most compliant model (FS = 0).

A qualitative comparison of the peak-systolic results, obtained for the rigid model and the aforesaid most compliant models, is shown in Figure 15. The first row presents distributions of WSS, in which high shear stress WSS ≥10 Pa is displayed in red. The fixed plaque zone is characterized by similar WSS in all cases, however, for both compliant approaches, mostly for the unsupported walls (FS = 0, E = 1 MPa), the non-physiological stress in the ECA is determined in significantly smaller regions than in the rigid-wall case. Wall-compliance affected also velocity fields, which are visible in the second and third rows, especially in the stenosis, which is a fixed one-sided narrowing of the canal. As

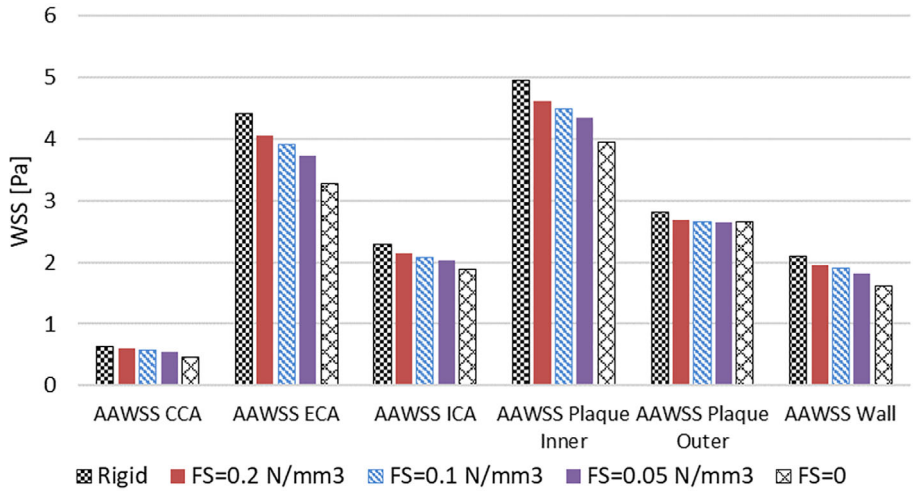

FIGURE 13 Comparison of time-averaged AAWSS obtained at the defined zones in transient simulations carried out with rigid-wall and fluid structure interaction approaches for selected values of foundation stiffness: FS = 0.2 N/mm^3, FS = 0.1 N/mm^3, FS = 0.05 N/mm^3, and FS = 0 (E = 1 MPa)

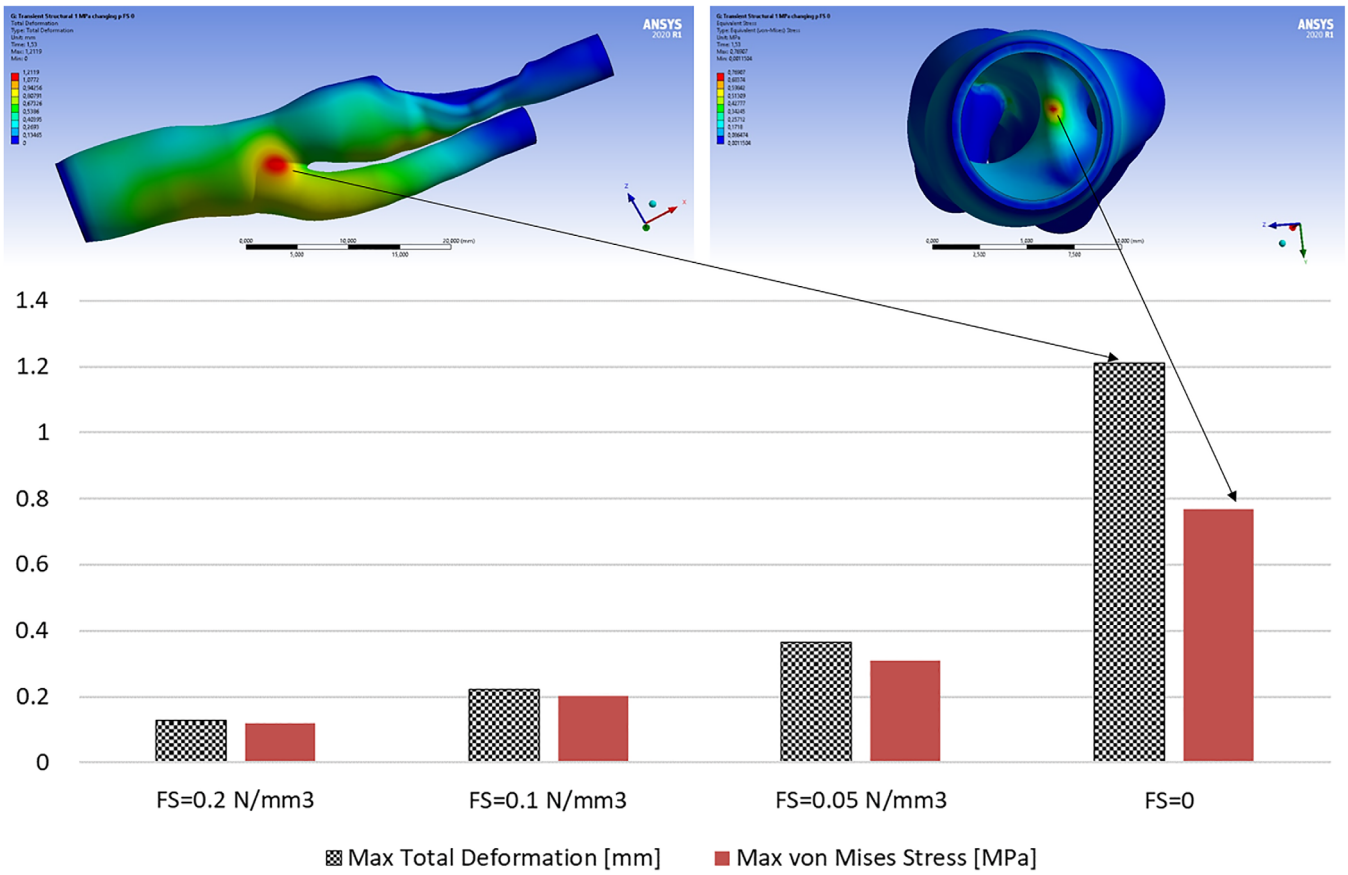

FIGURE 14 Comparison of peak-systolic deformation and stress in Wall determined in the structural domain in fluid structure interaction simulations for selected values of foundation stiffness: FS = 0.2 N/mm^3, FS = 0.1 N/mm^3, FS = 0.05 N/mm^3, and FS = 0 (E = 1 MPa)

velocity fields are associated with wall-resilience, it affects also dynamic viscosity (fourth row) that is a function of shear strain (fifth row) and vorticity (sixth row). Animations presenting changes in the distribution of the selected parameters over time can be found in Appendix S1.

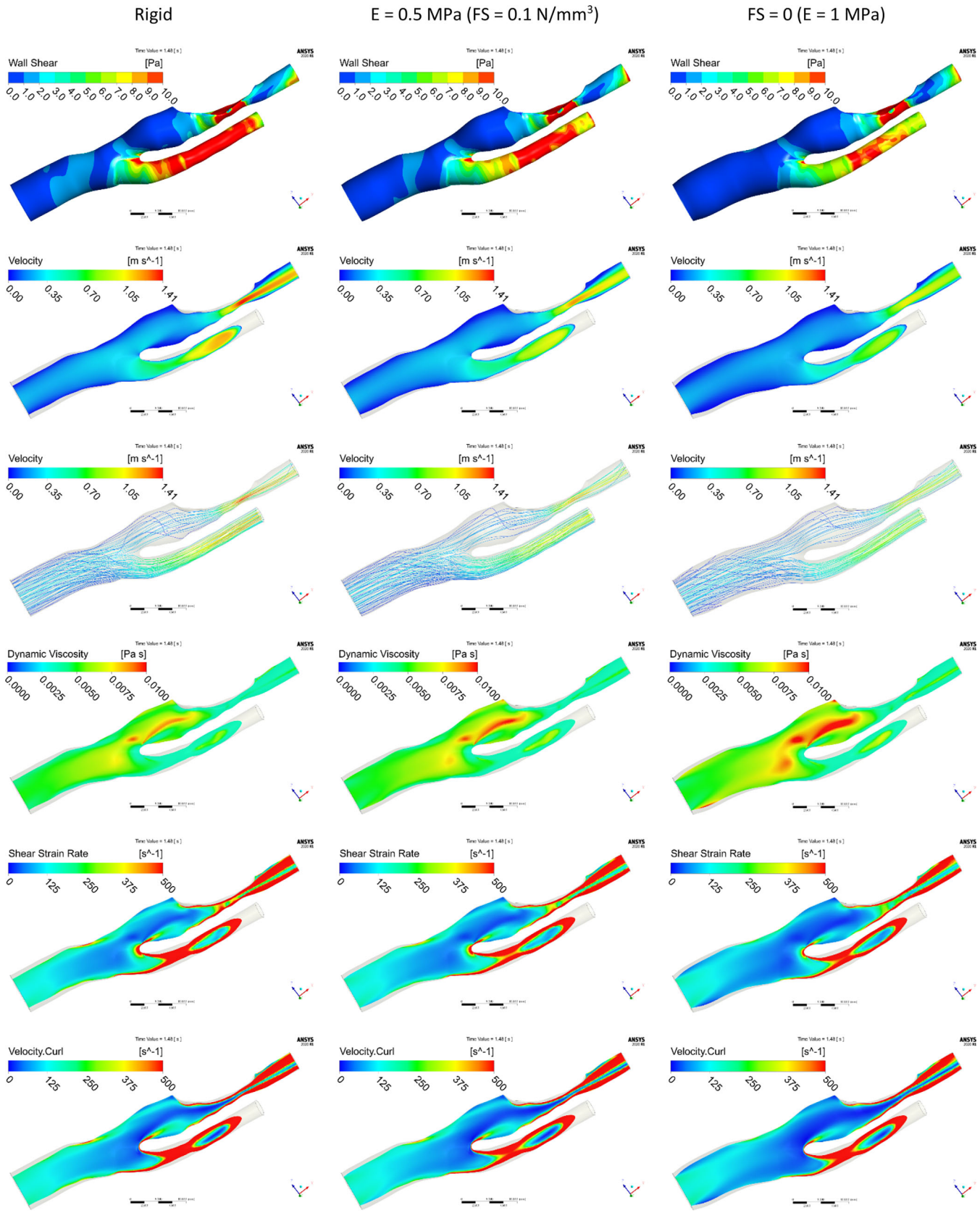

FIGURE 15 Distributions of peak-systolic parameters obtained with FSI and rigid-wall simulations in ANSYS CFX; the results are depicted in space (3D) or on the plane passing through the model (2D); from the top: WSS (3D), velocity (2D), streamlines (3D), dynamic viscosity (2D), shear strain rate (2D), and vorticity (2D). The same scales are used to allow one to compare the results in rows. Animations presenting changes in the distribution of the selected parameters over time can be found in the Appendix S1. FSI, fluid structure interaction; WSS, wall shear stress.

4 | DISCUSSION

This study shows the significance of the wall-compliant approach in numerical modeling of the blood flow through patient-specific symptomatic arterial stenosis that was operated on soon after obtaining medical images. The employed FSI technique provides more realistic results that are overestimated in rigid-wall simulations. This approach provides a deeper insight into the pathological hemodynamics in arterial stenosis that has been mostly analyzed in simplified models[46,47] or healthy carotid artery.[20,21] Due to the complicated geometry of the branch and stenosis, the flow was allowed to be turbulent in these zones. As the influence of blood rheology on the selected hemodynamic parameters was observed, the non-Newtonian model of blood was employed in FSI simulations in which dynamic effects associated with wall motion were additionally modeled. Similarly, the non-Newtonian approach was used in the study of near-wall phenomena in femoral stenosis.[47] To raise the spatial resolution of the presented simulations and to capture slight discrepancies between investigated cases a very precise numerical grid was generated in the fluid domain. Then, the sophisticated GCI test was performed to avoid discretization errors higher than 5% and to obtain Y plus parameter at the desired level (<2) in all simulations.

Similarly to others,[20,26] the elasticity-related wall-compliance was investigated with the FSI technique by means of selected values of Young's modulus. In FSI calculations with the lowest value of Young's modulus ($E = 0.5$ MPa), the peak-systolic maximal and time-averaged WSS are, respectively, 17% and 13% lower than in the rigid case ($E = \infty$), which is consistent with findings presented in References 16–18. However, additionally, this study provides other time-averaged hemodynamic parameters that are much lower in FSI than in the rigid-wall simulation (even 24% and 22% of the difference, respectively, for shear strain and vorticity for the high compliance in P5). As we hypothesize, these parameters can affect the symptoms of the patient and have not been reported before. Selected values of Young's modulus considerably influenced the response of the structural domain undergoing the same flow conditions. Differences between peak-systolic parameters obtained for $E = 3$ MPa and $E = 0.5$ MPa achieved 35% and 71%, respectively, for deformation and von Misses stress.

The foundation-related LCT compliance, neglected in other FSI studies, was investigated here with simulations in which different values of FS were used. The maximal discrepancies between the hemodynamic parameters obtained for the totally compliant walls (FS = 0) and stiff walls (FS = ∞) reached in this trial 43% (shear strain). For the high compliance, the peak-systolic maximal and time-averaged WSS achieved, respectively, 33% and 24% lower levels than in the rigid case. The FS coefficient influenced the structural domain behavior significantly, as the differences between peak-systolic parameters obtained for FS = 0 and FS = 0.2 N/mm^3 achieved 110% and 61%, respectively, for deformation and von Misses stress. Therefore, these findings allow us to state that local hemodynamics is strongly dependent on the compliance of LCT which was probably taken into account for the first time.

As concluded in,[25] elastic arterial wall simplifies the flow patterns and decreases the complexity of local flow profiles. This observation is confirmed here which can be clearly visible in stenosis (Figure 15). The lack of energy accumulation by the stiff walls results in the raised velocity that achieves lower values in both highly compliant cases (Figure 15). This fact affects the other hemodynamic quantities which are derived from velocity: WSS, shear strain rate, and vorticity. Due to the non-Newtonian model of blood rheology used in this study, blood viscosity, as dependent on velocity fields as well, is elevated in the environment of lower shear strain in the elastic models.

It cannot be left unmentioned that the results of each numerical investigation cannot be taken for granted due to oversimplification or spatiotemporal discretization errors. Thus, to prove the reliability of obtained data one has to compare them with patient-specific data obtained during patient's hospitalization, physiological values gathered during statistic-clinical case studies, or experimental data gathered on a specialized test rig that allows for investigating flows within physical phantoms. Concerning the latter method, e.g. experimental validation, one could utilize PIV (particle image velocimetry) measurements that allow for mapping the velocity vector field across the chosen cross-section of the model. Such an approach was successfully used in several researches where the authors investigated the influence of the stent presence in the arterial model[48,49] or where they investigated flows of Newtonian and non-Newtonian fluids in carotid artery bifurcation models with varying severity of the stenosis.[50] However, the main shortcoming of the PIV technique is related to the physical phantom, mainly its proper fabrication and preparation. Its structure has to be ideally transparent so that the laser beam can pass through its walls and be reflected from the flowing seeded particles, while the high-resolution camera can detect reflected light. Due to spatial constraints of the patient-specific models, they are usually prepared with a lost-wax method that results in preparation of a rigid phantom.[48,50] Concerning elastic models, they can be manufactured with specialized equipment (such as Material Jetting 3D printers), however, the exact values of their mechanical properties can vary significantly due to varied preparation processes and physic-

chemical reactions occurring during resin polymerization. Therefore, some scientists limit their experimental-numerical research to simplified geometries (Tomaszewski et al[49]). In our research, we analyzed varied (but with exact values) mechanical properties used during FSI simulations so we could not directly compare numerical results with experimental data. The mechanical properties of our phantoms might have not matched the exact values defined in the solver.

4.1 | Limitations

As compliance is associated not only with the wall elasticity but also with the reaction of the surrounding tissues, this factor must be somehow taken into consideration. In this paper, the response of LCT was modeled with arbitrarily chosen coefficients FS and was uniformly applied to the whole external wall of the model. This is a simplification and limitation of this study as the LCT reaction may be different for CCA supported by the carotid sheath and for more distal ICA entering the carotid canal in the temporal bone in the skull. Therefore, new experimental non-invasive methods allowing one to measure patient-specific mechanical properties of soft tissues in vivo are needed. Most of the research on stress–strain relation in the arterial tissues has been done on specimens dissected from human cadavers or animal models that differ from alive human tissues. Parallelly, hyperelastic and multilayered arterial models, which take into account plaque lesions, should be numerically investigated. Such analyses will provide a deeper insight into the wall behavior, and when combined with in vivo validation of hemodynamic parameters, they will allow finding the numerous unknown coefficients and factors with the use of reverse-engineering methods. Therefore, the development of micro-biosensors is also necessary.

5 | CONCLUSION

The paper clearly presents the importance of the assumption of wall-compliance in modeling blood flows through large arteries as it significantly influences the hemodynamic results if compared to the rigid-wall approach. In consequence, researchers have to face material model selection and the difficulty of defining the material properties of alive arterial tissues, which are patient-specific and basically unknown. Finally, the paper shows indirectly that stiff calcified plaque, which makes arterial walls rigid, significantly alters local hemodynamics. The study shows a huge increase in shear strain and vorticity in the stenotic zone which are usually not investigated in similar studies. This may be a reason for neurological symptoms and explains the positive effects of surgical removal of plaque allowing the blood flow parameters to achieve baseline values as in a healthy carotid artery.

ACKNOWLEDGMENTS

This project was financially supported by the Fund of Young Researchers granted by the Faculty of Mechanical Engineering at the Lodz University of Technology. The authors would like to thank student Meline Poissonnier for her help in the model reconstruction.

CONFLICT OF INTEREST

The authors declare no conflict of interest.

DATA AVAILABILITY STATEMENT

The data that supports the findings of this study are available in the supplementary material of this article.

ORCID

Daniel Jodko https://orcid.org/0000-0003-0107-838X
Zbigniew Tyfa https://orcid.org/0000-0001-9870-8370

REFERENCES

1. Caruso MV, Serra R, Perri P, et al. A computational evaluation of sedentary lifestyle effects on carotid hemodynamics and atherosclerotic events incidence. *Acta Bioeng Biomech*. 2017;19(3):43-52. doi:10.5277/ABB-00682-2016-03

2. Singh RB, Mengi SA, Xu Y-J, Arneja AS, Dhalla NS. Pathogenesis of atherosclerosis: A multifactorial process. *Exp Clin Cardiol*. 2002;7(1):40-53.
3. Wabnitz AM, Turan TN. Symptomatic carotid artery stenosis: surgery, stenting, or medical therapy? *Curr Treat Options Cardiovasc Med*. 2017;19(8):62. doi:10.1007/s11936-017-0564-0
4. Wafa HA, Wolfe CDA, Emmett E, Roth GA, Johnson CO, Wang Y. Burden of stroke in Europe: thirty-year projections of incidence, prevalence, deaths, and disability-adjusted life years. *Stroke*. 2020;51(8):2418-2427. doi:10.1161/STROKEAHA.120.029606
5. Kaźmierski P, Stelagowski M, Kasielska-Trojan A, Bogusiak K, Glabinski A. Neurologic and functional long-term outcome after carotid endarterectomy. *J Stroke Cerebrovasc Dis*. 2014;23(4):686-693. doi:10.1016/j.jstrokecerebrovasdis.2013.06.014
6. Chatzizisis YS, Coskun AU, Jonas M, Edelman ER, Feldman CL, Stone PH. Role of endothelial shear stress in the natural history of coronary atherosclerosis and vascular remodeling. Molecular, cellular, and vascular behavior. *J Am Coll Cardiol*. 2007;49(25):2379-2393. doi:10.1016/j.jacc.2007.02.059
7. Chiu J-J, Chien S. Effects of disturbed flow on vascular endothelium: pathophysiological basis and clinical perspectives. *Physiol Rev*. 2011;91(1):327-387. doi:10.1152/physrev.00047.2009
8. Dolan JM, Kolega J, Meng H. High wall shear stress and spatial gradients in vascular pathology: A review. *Ann Biomed Eng*. 2013;41(7):1411-1427. doi:10.1007/s10439-012-0695-0
9. Stone PH, Coskun AU, Lucier M, et al. Intravascular hemodynamics and coronary artery disease: new insights and clinical implications. *Hell J Cardiol*. 2016;57(6):389-400. doi:10.1016/j.hjc.2016.11.019
10. Humphrey JD, Schwartz MA. Vascular mechanobiology: homeostasis, adaptation, and disease. *Annu Rev Biomed Eng*. 2021;23:1-27. doi:10.1146/annurev-bioeng-092419-060810
11. Gharahi H, Zambrano BA, Zhu DC, DeMarco J, Baek S. Computational fluid dynamic simulation of human carotid artery bifurcation based on anatomy and volumetric blood flow rate measured with magnetic resonance imaging. *Int J Adv Eng Sci Appl Math*. 2016;8:46-60.
12. Polanczyk A, Podgorski M, Wozniak T, Stefanczyk L, Strzelecki M. Computational fluid dynamics as an engineering tool for the reconstruction of hemodynamics after carotid artery stenosis operation: A case study. *Medicina (Lithuania)*. 2018;54(3):1-15. doi:10.3390/medicina54030042.
13. Reorowicz P, Obidowski D, Klosinski P, Szubert W, Stefanczyk L, Jozwik K. Numerical simulations of the blood flow in the patient-specific arterial cerebral circle region. *J Biomech*. 2014;47(7):1642-1651. doi:10.1016/j.jbiomech.2014.02.039
14. Tyfa Z, Obidowski D, Reorowicz P, Stefańczyk L, Fortuniak J, Jóźwik K. Numerical simulations of the pulsatile blood flow in the different types of arterial fenestrations: comparable analysis of multiple vascular geometries. *Biocybern Biomed Eng*. 2018;38(2):228-242. doi:10.1016/j.bbe.2018.01.004
15. Starmans-Kool MJ, Stanton AV, Zhao S, Yun XX, Thom SAM, Hughes AD. Measurement of hemodynamics in human carotid artery using ultrasound and computational fluid dynamics. *J Appl Physiol*. 2002;92(3):957-961. doi:10.1152/japplphysiol.00171.2001
16. McGah PM, Leotta DF, Beach KW, Aliseda A. Effects of wall distensibility in hemodynamic simulations of an arteriovenous fistula. *Biomech Model Mechanobiol*. 2014;13(3):679-695. doi:10.1007/s10237-013-0527-7
17. Decorato I, Kharboutly Z, Legallais C, Salsac AV. Numerical study of the influence of wall compliance on the haemodynamics in a patient-specific arteriovenous fistula. *Comput Methods Biomech Biomed Engin*. 2011;14(sup1):121-123. doi:10.1080/10255842.2011.593762
18. Decorato I, Kharboutly Z, Vassallo T, Penrose J, Legallais C, Salsac AV. Numerical simulation of the fluid structure interactions in a compliant patient-specific arteriovenous fistula. *Int J Numer Meth Biomed Eng*. 2014;30(2):143-159. doi:10.1002/cnm.2595
19. Kumar N, Khader SMA, Pai R, Khan SH, Kyriacou PA. Fluid structure interaction study of stenosed carotid artery considering the effects of blood pressure. *Int J Eng Sci*. 2020;154:103341. doi:10.1016/j.ijengsci.2020.103341
20. Lopes D, Puga H, Teixeira JC, Teixeira SF. Influence of arterial mechanical properties on carotid blood flow: comparison of CFD and FSI studies. *Int J Mech Sci*. 2019;160:209-218. doi:10.1016/j.ijmecsci.2019.06.029
21. Sousa LC, Castro CF, António CC, Azevedo E. Fluid-structure interaction modeling of blood flow in a non-Stenosed common carotid artery bifurcation. Proceedings of the 7th International Conference on Mechanics and Materials in Design, June 11-15, 2017; Albufeira/Portugal. 1559-1564.
22. Johnston BM, Johnston PR, Corney S, Kilpatrick D. Non-Newtonian blood flow in human right coronary arteries: transient simulations. *J Biomech*. 2006;39(6):1116-1128. doi:10.1016/j.jbiomech.2005.01.034
23. Soulis JV, Giannoglou GD, Chatzizisis YS, Seralidou KV, Parcharidis GE, Louridas GE. Non-Newtonian models for molecular viscosity and wall shear stress in a 3D reconstructed human left coronary artery. *Med Eng Phys*. 2008;30(1):9-19. doi:10.1016/j.medengphy.2007.02.001
24. Jozwik K, Obidowski D. Numerical simulations of the blood flow through vertebral arteries. *J Biomech*. 2010;43(2):177-185. doi:10.1016/j.jbiomech.2009.09.026
25. Chen X, Zhuang J, Huang H, Wu Y. Fluid–structure interactions (FSI) based study of low-density lipoproteins (LDL) uptake in the left coronary artery. *Sci Rep*. 2021;11(1):1-12. doi:10.1038/s41598-021-84155-3
26. Cho KC, Yang H, Kim JJ, Oh JH, Kim YB. Prediction of rupture risk in cerebral aneurysms by comparing clinical cases with fluid–structure interaction analyses. *Sci Rep*. 2020;10(1):1-8. doi:10.1038/s41598-020-75362-5
27. Kafi O, El Khatib N, Tiago J, Sequeira A. Numerical simulations of a 3D fluid-structure interaction model for blood flow in an atherosclerotic artery. *Math Biosci Eng*. 2017;14(1):179-193. doi:10.3934/mbe.2017012
28. Holzapfel GA, Ogden RW. Constitutive modelling of arteries. *Proc R Soc A: Mat Phys Eng Sci*. 2010;466(2118):1551-1597. doi:10.1098/rspa.2010.0058

29. Gasser TC, Ogden RW, Holzapfel GA. Hyperelastic modelling of arterial layers with distributed collagen fibre orientations. *J R Soc Interface*. 2006;3(6):15-35. doi:10.1098/rsif.2005.0073
30. Jayendiran R, Nour B, Ruimi A. Computational fluid–structure interaction analysis of blood flow on patient-specific reconstructed aortic anatomy and aneurysm treatment with Dacron graft. *J Fluids Struct*. 2018;81:693-711. doi:10.1016/j.jfluidstructs.2018.06.008
31. Bukala J, Kwiatkowski P, Malachowski J. Numerical analysis of stent expansion process in coronary artery stenosis with the use of non-compliant balloon. *Biocybern Biomed Eng*. 2016;36(1):145-156. doi:10.1016/j.bbe.2015.10.009
32. Corpataux J-M. Low-pressure environment and remodelling of the forearm vein in Brescia-Cimino haemodialysis access. *Nephrol Dial Transplant*. 2002;17(6):1057-1062. doi:10.1093/ndt/17.6.1057
33. Kojo M, Yamada K, Izumi T. Normal developmental changes in carotid artery diameter measured by echo-tracking. *Pediatr Neurol*. 1998;18(3):221-226. doi:10.1016/S0887-8994(97)00195-1
34. Studinger P, Lénárd Z, Kováts Z, Kocsis L, Kollai M. Static and dynamic changes in carotid artery diameter in humans during and after strenuous exercise. *J Physiol*. 2003;550(2):575-583. doi:10.1113/jphysiol.2003.040147
35. Torii R, Oshima M, Kobayashi T, Takagi K, Tezduyar TE. Influence of wall elasticity in patient-specific hemodynamic simulations. *Comput Fluids*. 2007;36(1):160-168. doi:10.1016/j.compfluid.2005.07.014
36. Jodko DM, Obidowski DS, Reorowicz P, Jóźwik K. A two-stage model of an arteriovenous fistula maturation process. *Acta Bioeng Biomech*. 2020;22(2):139-153. doi:10.37190/ABB-01571-2020-02
37. Bukała JK, Małachowski J, Kwiatkowski P. Finite element analysis of the percutaneous coronary intervention in a coronary bifurcation. *Acta Bioeng Biomech*. 2014;16(4):24-31. doi:10.5277/ABB-00041-2014-02
38. Celik IB, Ghia U, Roache PJ, Freitas CJ, Coleman H, Raad PE. Procedure for estimation and reporting of uncertainty due to discretization in CFD applications. *J Fluids Eng Trans ASME*. 2008;130(7):780011-780014. doi:10.1115/1.2960953
39. Browne LD, Walsh MT, Griffin P. Experimental and numerical analysis of the bulk flow parameters within an arteriovenous fistula. *Cardiovasc Eng Technol*. 2015;6(4):450-462. doi:10.1007/s13239-015-0246-6
40. Jodko D, Obidowski D, Reorowicz P, Jóźwik K. Blood flows in end-to-end arteriovenous fistulas: unsteady and steady state numerical investigations of three patient-specific cases. *Biocybern Biomed Eng*. 2017;37(3):528-539. doi:10.1016/j.bbe.2017.05.006
41. ANSYS Release 2020 R1. CFX-Solver Theory Guide. U.S.A. 2020.
42. Menter FR. Two-equation eddy-viscosity turbulence models for engineering applications. *AIAA J*. 1994;32(8):1598-1605. doi:10.2514/3.12149
43. ANSYS Release 2020 R1. Mechanical User's Guide. U.S.A. 2020.
44. Malazi MT, Eren ET, Luo J, Mi S, Temir G. Three-dimensional fluid-structure interaction case study on elastic beam. *J Marine Sci Eng*. 2020;8(9):1-21. doi:10.3390/JMSE8090714
45. ANSYS Release 2020 R1. System Coupling Settings and Commands Reference. U.S.A. 2020.
46. Papadakis G, Raspaud J. Wave propagation in stenotic vessels; theoretical analysis and comparison between 3D and 1D fluid–structure-interaction models. *J Fluids Struct*. 2019;88:352-366. doi:10.1016/j.jfluidstructs.2019.06.003
47. Barber T. Wall shear stress and near-wall flows in the stenosed femoral artery. *Comput Methods Biomech Biomed Engin*. 2017;20(10):1048-1055. doi:10.1080/10255842.2017.1331342
48. Li Y, Verrelli DI, Yang W, Qian Y, Chong W. A pilot validation of CFD model results against PIV observations of haemodynamics in intracranial aneurysms treated with flow-diverting stents. *J Biomech*. 2020;13(100):109590. doi:10.1016/j.jbiomech.2019.109590
49. Tomaszewski M, Sybilski K, Baranowski P, Małachowski J. Experimental and numerical flow analysis through arteries with stent using particle image velocimetry and computational fluid dynamics method. *Biocybern Biomed Eng*. 2020;40(2):740-751. doi:10.1016/j.bbe.2020.02.010
50. DiCarlo AL, Holdsworth DW, Poepping TL. Study of the effect of stenosis severity and non-Newtonian viscosity on multidirectional wall shear stress and flow disturbances in the carotid artery using particle image velocimetry. *Med Eng Phys*. 2019;1(65):8-23. doi:10.1016/j.medengphy.2018.12.023

SUPPORTING INFORMATION

Additional supporting information may be found in the online version of the article at the publisher's website.

How to cite this article: Jodko D, Jeckowski M, Tyfa Z. Fluid structure interaction versus rigid-wall approach in the study of the symptomatic stenosed carotid artery: Importance of wall compliance and resilience of loose connective tissue. *Int J Numer Meth Biomed Engng*. 2022;38(8):e3630. doi:10.1002/cnm.3630